# Advancing diffusion MRI: improving image quality and getting rid of the fat

Dong, Y.

# Chapter 1

## Introduction

## 1.1 Diffusion MRI - general view

Since the creation of the first Nuclear Magnetic Resonance (NMR) image by Paul Lauterbur[1] in 1973, Magnetic Resonance Imaging (MRI), has evolved tremendously within the past half-century[2]. Thus, MRI, as a noninvasive and non-ionizing radiation involving modality, transformed the entire field of medical imaging, next to X-ray, CT and PET, significantly. Thus, MRI is being indispensable in today's medical diagnostics and therapy follow up.

MRI is very famous for the many different soft tissue contrasts that can be realized, and water, the most abundant molecule in the human body, plays a very important role in there. The human body consists of roughly 60% water which is, as a key component, involved in many structural and functional processes, which are influenced by its local environment and altering thus its MR relaxation behavior. This variation in relaxation properties largely contributes to the huge variety of tissue contrasts, allowing detailed and specific diagnostic imaging of different body structures, functions and states.

Among those many clinically useful contrasts, diffusion MRI[3–6] stands out for its unique ability to non-invasively measure the microscopic movement of water molecules within tissue. Diffusion MRI utilizes the abundance of the water molecule, inherent in the human body, as natural reporter molecule, providing a window on the microstructure of tissue. This microscopic movement, or diffusion, provides invaluable insight into the cellular structure and state of tissues, which is critical to understanding and diagnosing various pathologies[7].

In physics, diffusion is defined as the random thermal movement of molecules, a process that is particularly relevant to water molecules in biological tissues. For illustration, consider a drop of ink dispersed in a glass of water: the ink will spread isotopically, eventually staining the entire glass in the end. This analogy helps to understand diffusion MRI in medical imaging, where analysis of how water molecules diffuse through tissue provides insight into its microstructural properties[4]. These characteristics often change in certain disease states, thus diffusion MRI can detect such subtle changes at the cellular level, often before they are visible with other imaging techniques[8]. For example, in tumors showing chaotic cell growth or accumulation of unfinished proteins within the cells, water diffusion can be hindered and restricted. As more dense cellular structures hamper the movement of water molecules, diffusion weighted MRI can readily detect this change (e.g., prostate cancer[9–11]). Thus, the ability to detect small changes in water diffusion makes diffusion MRI an invaluable tool for

the early detection and characterization of disease, which is important for diagnose, treatment planning and monitoring response to therapy.

A basic technique is diffusion-weighted imaging[3,4] (DWI), which measures the diffusion of water molecules by special MR sequences involving the use of diffusion sensitizing gradients, highlighting areas of diffusion alteration, indicative of various lesions, in a qualitative manner by changing the contrast in the images.

However, diffusion MRI allows also quantification of diffusion resulting in maps of the apparent diffusion coefficient (ADC)[4]. The term "apparent" is used, because the calculated diffusion coefficients are influenced by several factors beyond "pure" diffusion. These include perfusion, partial volume effects, and experimental errors[12], all of which can affect the accuracy of the measurement. Nevertheless, the ADC remains an important quantitative tool that maps the diffusion of water molecules in complex cellular environments.

While ADC provides a summary parameter that assumes diffusion is isotropic, measuring the anisotropy of diffusion can be highly informative, especially in tissues organized as fibers where diffusion differs for different directions. Examples of tissues with significant anisotropy include brain white matter[3,13], nerves and skeletal muscle[14,15]. Diffusion Tensor Imaging (DTI[7]) advances the principles of DWI by measuring and modeling the multidimensional character of water diffusion. It involves applying diffusion sensitizing gradients in many different orientations during the measurements and fitting the results to corresponding tensor models[3,7,16]. This aspect of DTI is particularly valuable, e.g., in the studies of white matter tracts in the brain[13], improving the researcher’s understanding of neuroanatomy, neurodegenerative diseases and other neurological conditions[3].

Today, diffusion MRI shows a great amount of important clinical applications. For instance, for the brain, it is critical for the early detection of stroke[17], for the characterization of tumors[18], and for the assessment of neurodegenerative diseases[19]. Beyond the brain, it has shown great promise, e.g., in the head-neck region[20], it helps evaluate microstructural changes in various pathologies, helps to distinguish between benign and malignant lesions, and is important for monitoring the effectiveness of treatments. In the prostate[9], diffusion MRI has become an integral part of the multi-parametric MRI approach[21], improving the detection and risk stratification of prostate cancer. Diffusion MRI in the liver has also shown effectiveness for tissue characterization, tumor assessment and disease prognosis[22].

## 1.2 Diffusion sensitized MRI - a more technical overview

In 1965, Stejskal and Tanner[23] conducted initial NMR experiments incorporating diffusion weighting through an additional pair of motion sensitizing gradients (Figure 1.1). These gradients, known as Stejskal–Tanner gradients, are still widely used in standard diffusion-weighed sequences today.

The purpose of using these two gradients in DWI is to attenuate the transverse magnetization by the mechanisms of dephasing and diffusion-induced incomplete rephasing. The first diffusion-sensitizing gradient induces dephasing by creating spatially varying phase differences between water signals at different locations. For ideal stationary water with no movements, the second gradient reverses these additional phases, preserving the original magnetization (see Fig.1.1) [8]. However, when water moves between these two gradients (e.g., when diffusion happens along the sensitizing direction), they experience different magnetic fields, which impacts the ability of the second gradient to completely rephase the dephasing effect of the first one. This incomplete rephasing manifests itself as signal attenuation, a surrogate marker of molecular diffusion. Typically, diffusion-sensitizing gradients are positioned symmetrically around a refocusing (180°) RF pulse (Stejskal–Tanner set-up), as shown in Figure 1.1. As a measure for the diffusion sensitization, the b-value can be calculated based on the gradient's amplitude ($g_D$), duration ($\delta$), and the time interval ($\Delta$) between the two diffusion-sensitizing gradients[8]:

$$b = (\gamma \cdot g_D \cdot \delta)^2 \cdot \left(\Delta - \frac{\delta}{3}\right), \quad (1)$$

where $\gamma$ represents the gyromagnetic ratio. The b-value is a parameter that reflects the strength and timing of the gradients applied to create such diffusion-weighted contrast. Higher b-values means stronger diffusion effects might be captured. The b-value is typically chosen in a range between[8] 50-2000 s/mm², although higher b-values may be utilized for specialized applications[24]. Achieving these b-values necessitates the use of relatively long and strong diffusion sensitizing gradients.

In this context, ADC mapping is achieved by fitting an exponential curve to a series of DW images, measured at multiple b-values. The signal model used for fitting depends on the application with the simplest one assuming a mono-exponential decay[8]:

$$S_b = S_0 e^{-bD}, \tag{2}$$

where $S_0$ is the signal intensity at baseline (conventionally at b=0 s/mm$^2$), $S_b$ is the signal at a given b-value $b$, $D$ is the apparent ADC value to be fitted for a given pixel. Model selection can also vary depending on the application and can become very complicated, especially when factors such as perfusion effects are included[25]. In a clinical setting, ADC maps are highly informative. Typically, lower ADC values are indicative for increased tissue cellularity, a common feature of various tumors and pathological conditions.

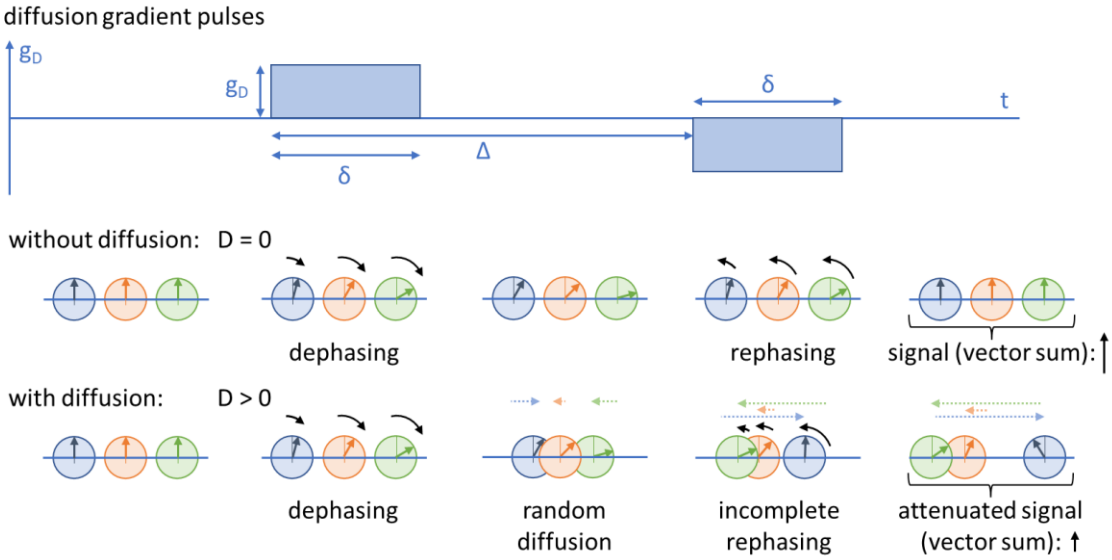


**Figure 1.1.** The effect of diffusion-sensitizing gradients. The first gradient dephases three "labeled spins" (represented by blue/orange/green arrows at different positions). If they remain stationary (D=0), a second gradient of opposite sign completely rephases them. However, if they diffuse between the gradients (D>0), the rephasing is incomplete, resulting in a diffusion-weighted signal attenuation, as shown by the "vector sum" arrows representing the remaining magnetization.

## 1.3 Echo planar imaging (EPI)

In 1983, one of the most important MRI sequences, known as Echo Planar Imaging (EPI)[26,27], was introduced by Peter Mansfield that revolutionized the field of MRI with its rapid acquisition capabilities. A key feature of single-shot EPI (ssh-EPI) is its inherent ability to "freeze" the subject's motion. This is achieved by its zigzag trajectory, which allows to efficiently sample the entire k-space within one acquisition window, typically ranging from 30 to 100 ms per slice, allowing to reconstruct a complete image from those data. This capability has not only made ssh-EPI to a preferred choice in various imaging scenarios (e.g. in quantitative MRI[28] and fMRI[29]) but has also established it as a standard technique for

DWI[3,18]. To further accelerate the acquisition, parallel imaging techniques[30,31], can also be integrated with the ssh-EPI. For such a cartesian EPI trajectory, the under-sampling could simply be done by skipping multiple phase encoding lines in an interleaved fashion and using the redundant multi-element coil information for proper reconstruction[30,31].

Despite its advantages in fast acquisition, ssh-EPI has several limitations due to prevalent artifacts that significantly affect image quality. These include Nyquist ghosting, $T_2$* blurring, geometric image distortion, and chemical shift effects (spatially displaced fat signals), which may require further correction (Figure 1.2)[32].

**Nyquist Ghosting:** Typically caused by gradient hardware-related (eddy-currents or gradient transfer function induced) odd-even echo misalignment[33]. Nyquist ghosting is addressed by realigning the k-space data during image reconstruction. This alignment is accomplished (in most cases) by performing additional EPI reference scans to measure the phase differences between the odd/even lines in k-space.

**$T_2$* blurring:** This artifact is primarily attributed to $T_2$* decay, which results in pronounced signal loss in the outer regions of k-space corresponding to high spatial frequencies which may lead to image blur. To reduce $T_2$* blurring, it is critical to use a short readout window to minimize the time for $T_2$* decay to affect the signal. For mitigation, parallel imaging[30,31] with high acceleration factors can be used or the single-shot sequence is split into multi-shot EPI[34–36] which needs further special consideration (see chapters 2-7).

**Geometric Distortion:** A typical artifact in ssh-EPI, like geometric distortion, occurs often in areas with severe inhomogeneities in the main magnetic field ($B_0$ field), for example near tissue-air interfaces, where tissue susceptibility changes rapidly. In ssh-EPI, the intrinsic low bandwidth in the phase encoding direction leads to high geometric distortions that are particularly difficult to correct. Several strategies have been proposed to deal with this problem. For example, parallel imaging techniques could help to increase the bandwidth of ssh-EPI along the phase encoding direction (e.g. SENSE[28] and GRAPPA[30,31]). Moreover, approaches such as blip-up/blip-down (BUDA)[37] acquisition, multi-shot interleaved-EPI[34,38,39], and read-out-segmented EPI[40], are frequently used to mitigate it.

**Displaced fat signals:** This artifact is caused by the resonance frequency differences between water and fat[41] (called water-fat or chemical shift, described in more detail in Section 1.4) and is mainly due to the low bandwidth in the phase encoding direction of the EPI. To

eliminate the resulting fat displacement artifacts, several fat suppression techniques (e.g. STIR[42], SPIR[43], and SPAIR[44]) are used.

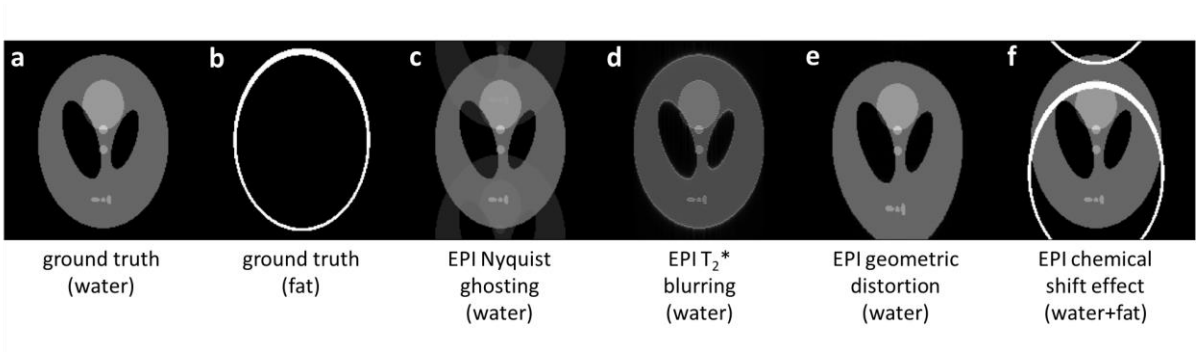


**Figure 1.2.** Typical artifacts in EPI sequences. The figure shows four different "typical" EPI artifacts as Nyquist ghosting, $T_2$* blurring, geometric distortion, and chemical shift effects of fat. (a-b) Water and fat ground truth images are displayed as reference. Except for the last image containing both water and fat, the fat signal has been assumed completely suppressed in the water-only examples to highlight the associated artifacts. (c) Nyquist ghosting (also referred to as N/2 ghosting) shows up as duplicate, weakly superimposed images along phase encoding direction. (d) $T_2$* blur is shown as a loss of image sharpness and resolution (especially at phantom edges). (e) Geometric distortions manifest as deformations such as image warping, stretching or compression, reflecting severe localized inhomogeneities in the $B_0$ field. (f) Chemical shift effects of fat are shown as a spatial displacement of the fat signal relative to the water, along the phase encoding direction.

Multi-shot interleaved EPI[34–36,38,39] (msh-EPI) has emerged as a potential alternative to ssh-EPI, particularly in diffusion-weighted imaging (DWI), due to its ability to minimize geometric distortions and $T_2$* blurring while achieving high signal-to-noise ratio (SNR) and spatial resolution. However, for clinical DWI scans, ssh-EPI are still often the preferred sampling approach due to its robustness against motion artifacts. DWI exploits the random small-scale motion of the water molecules to generate diffusion contrast (c.f. Fig.1.1), using paired diffusion-sensitizing gradients. The effect on the MRI-signal of those gradients are very sensitive by nature also to macroscopic motion[45,46]. Therefore, even physiological motion, such as cardiac pulsation or respiration, can introduce significant phase variations unrelated to diffusion, posing a typical challenge to msh-EPI[32]. A correction to preserve the proper phase information for accurate image reconstruction from multiple acquisitions is therefore required. If these motion-induced phase inconsistencies are not addressed, severe aliasing / ghosting will occur, compromising the diagnostic value of the resulting images seriously.

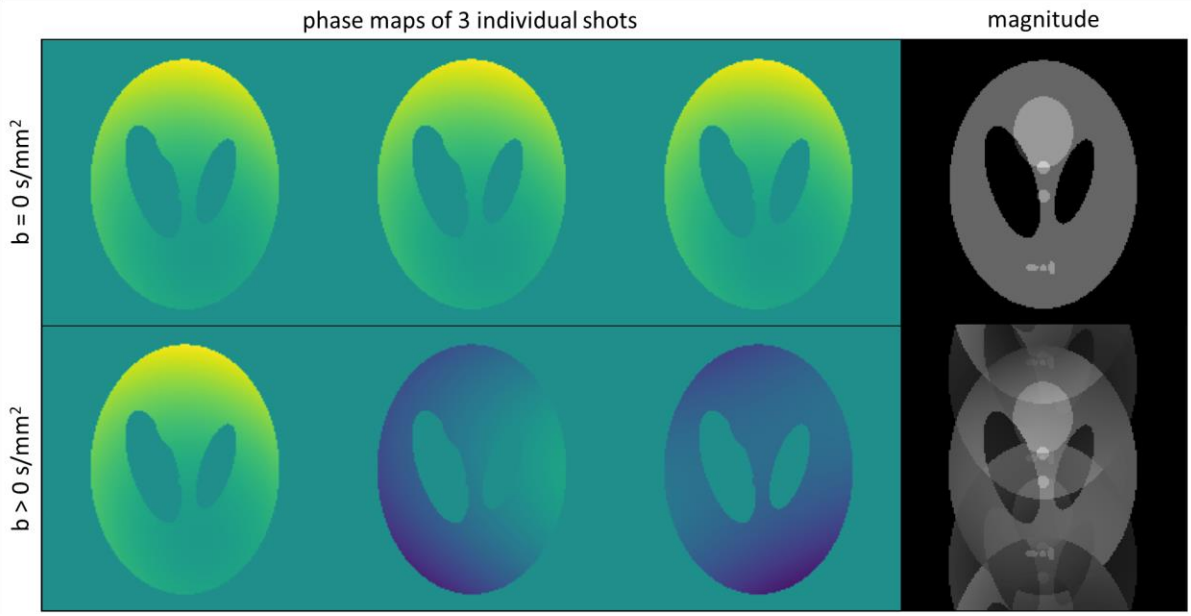


**Figure 1.3.** Simulated phantom data of a multi-shot EPI scan, without (b=0s/mm²) / with (b>0s/mm²) diffusion contrast. The shot-to-shot phase variations, resulting from rather small gross motion effects, require specific correction to reconstruct aliasing-free magnitude images.

Several strategies have been developed to address these challenges of msh-EPI. One common approach is to use additional k-space measurements as low-resolution navigators[39,] helping to track and correct the phase variations between different shots during image reconstruction. Alternatively, motion-induced phase maps can be estimated for each shot from the imaging data itself via self-navigated reconstruction[47,48]. Recently, researchers have introduced promising techniques such as locally low-rank reconstruction[49,50] in image space and structured low-rank[51,52] approaches in k-space to reconstruct DW msh-EPI data with high quality. These methods allow joint reconstruction of the complex-valued images from different shots through matrix completion, exploiting the redundancy of information across shots for a high-quality, navigator-free reconstruction. In most of these techniques, parallel imaging[30,31] plays an important role by providing an additional dimension of data redundancy (i.e., the multi-element coil dimension) to support the image reconstruction. The basic principles and practical applications of all these techniques will be described and discussed in detail in this thesis.

## 1.4 Fat in MRI

Hydrogen protons in water and fat, the two most abundant molecules present in the human body, have inherently different chemical properties[53]. This makes them also to have different magnetic properties when exposed in strong magnetic fields like in MRI, resulting in

different MR spectra due to the different chemical shifts of the observed protons. The water molecule consists of one oxygen and two chemically equivalent hydrogen atoms. This results in a single line proton spectrum at a certain specific resonance frequency. Specific electronic environments affect the magnetic properties of the hydrogen protons in different ways, which become clear when considering fat (mainly present in the form of long-chain triglycerides) and its resonance spectrum. The fat triglycerides consist of a glycerol backbone and three fatty acid chains, each containing many carbon and hydrogen atoms[53,54]. In this case, the electron clouds, forming the chemical bounds between carbon and hydrogen atoms in the fatty acid chains, act as a shield, changing the local magnetic field experienced by the individual hydrogen protons. This results in molecule-site specific hydrogen proton resonance frequencies, forming the fat spectrum with multiple peaks representing the different proton sites. Thus, the MR fat spectrum looks more complicated than the single line water proton signal. In short, each molecule has its characteristic MR spectrum, which could function as the molecules fingerprint for identification.

The concept of "chemical shift" in MRI is based on this “off-resonance” in frequency. It should also be noted that due to the different molecular structures of each fat subcomponent, fat in human tissues has a multi-peak spectrum, as shown in Figure 1.4.

In many MRI applications, researchers and clinicians are only interested in water tissue, so the fat signal is just a confounding factor that needs to be removed. Several different fat suppression techniques have been developed to suppress the fat signals, such as STIR (Short Tau Inversion Recovery)[42], SPIR (Spectral Pre-saturation with Inversion Recovery)[43], and SPAIR (SPectral Attenuated Inversion Recovery)[44]. However, SPIR and SPAIR are very sensitive to another off-resonance effect, the limited main field ($B_0$) homogeneity, which may strongly compromise the effectiveness and quality of fat suppression. In addition, SPIR and STIR are sensitive to $B_1^+$ inhomogeneities, which may lead to incomplete fat suppression or even unwanted loss of the water signal, which is particularly undesirable in diffusion MRI, where the SNR of water images is very limited. As a good alternative, the Dixon[55–58] method, based on chemical shift encoding, attempts to utilize the “chemical shift” properties to distinguish between water and fat by "decoding" these two tissue components as well as the $B_0$ inhomogeneity from the MRI-signal measured at slightly shifted echo-times. This joint estimation can then be achieved by solving the encoding system in a least-square sense and calculating both the water, fat images and the $B_0$ map, simultaneously[58].

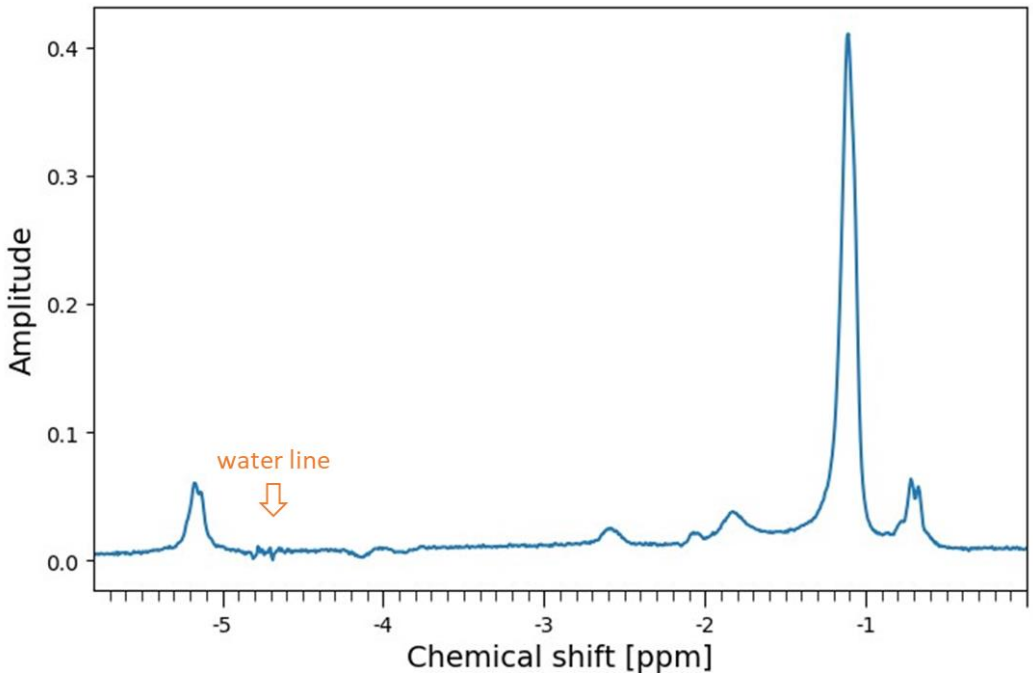


**Figure 1.4.** MR fat spectrum collected from a single voxel in bone marrow of one subject's leg at 3T using STEAM[59] sequence at TE=60 ms. The different resonances belong to the different hydrogen protons located in different chemical environments within the fat molecule. The spectrum's magnitude also varies with the measured TE, reflecting changes in signal intensity at different TEs. The location of water line in the spectrum is marked with an orange arrow. Often, for fat suppression and simplicity the fat spectrum is considered to consist out of a single line. In diffusion this might be considered an oversimplification resulting in artefacts due to residual fat signal from unsuppressed peaks.

In diffusion MRI, there is always a need to suppress the fat signals for many reasons. Especially when using EPI, this is the case. Due to the low bandwidth in the phase-encoding direction, chemical shift effects can lead to a substantial spatial displacement of fat, so that it can cover important water signals, as shown in Figure 1.2. A second reason is that fat, being a large molecule, always exhibits limited diffusion. As a result, the fat signal will not be attenuated as much by the diffusion encoding process as water-signals will be and will therefore be overshadowing the water signal at high b-value images (even when only all the minor peaks as shown in Fig 1.4 provide signal), thus interfering with the interpretation of the water diffusion signal.

## 1.5 Outline

This thesis focuses on improving the image quality of DWI, especially in applications outside the brain. To achieve this, it proposes a combination of (1) multi-shot EPI, which provides

high-resolution, high-SNR and less geometric distortion DWI images compared to single-shot EPI, and (2) Dixon-based water-fat separation, which allows effective fat signal suppression for multiple peaks of the fat spectrum. However, it is inherently challenging to jointly account for multiple nonlinear phase terms in the reconstruction because one has to deal with fat off-resonance-induced phase offsets, the $B_0$ inhomogeneities, the shot-to-shot motion-induced diffusion phase variations and many other experimental issues. The thesis addresses these challenges step by step by developing, optimizing, and testing different algorithms, verifying the underlying assumptions in-vivo, in small volunteer studies.

**Chapter 2** focuses on replacing the fat saturation by an efficient chemical shift encoding (Dixon) approach in the image acquisition and the development of an algorithm for water/fat separation in multi-shot EPI. The image reconstruction addresses the chemical shift effects, the spatial displacement of fat signals, and the joint water/fat and $B_0$ map estimation, whereas a 2D extra navigator approach is used for phase navigation and corresponding phase correction in the DWI image reconstruction.

**Chapter 3** explores an alternative water/fat separation for EPI using coil sensitivity information as a virtual SENSE[60] problem. Here one takes advantage of the spatial shift of the fat signals in the image domain that can support disentangling water and fat signals in EPI.

**Chapter 4** improves the Dixon-based approach of chapter 2 with a model-based water/fat separation algorithm, employing phase self-navigation to replace the measured 2D-navigator. This is a substantial step forward to make the DW sequence much more time efficient, doing without the time-consuming fat-suppression and extra navigator.

**Chapter 5** demonstrates the potential to correct macroscopic motion using spatial information from the fat signal. Leveraging the fat as an additional source of information, instead of just suppressing it to begin with seems to be an interesting concept with many more applications.

**Chapter 6** describes the application of an advanced regularization scheme that uses the redundant information in the receive channel and shot domain of the acquired data. Using structured low-rank concepts for the joint water/fat estimation, the image quality is improved through Hankel matrix completion and offers interesting data under-sampling strategies.

**Chapter 7** applies this low-rank based water/fat separation algorithm to improve prostate DWI by reducing geometric distortion while maintaining diagnostic image quality. The concept is validated by comparing Dixon multi-shot EPI with an established single-shot EPI protocol. In this work also different applications for using the separately reconstructed fat image are discussed.

Finally, **Chapter 8** provides a general discussion of all the proposed algorithms and results and explores the remaining challenges and future research directions.

## References


1. Lauterbur PC. Image formation by induced local interactions: Examples employing nuclear magnetic resonance. *Nature*. 1973;242(5394).

2. Börnert P, Norris DG. A half-century of innovation in technology-preparing MRI for the 21st century. *British Journal of Radiology*. 2020;93(1111).

3. Huisman TAGM. Diffusion-weighted and diffusion tensor imaging of the brain, made easy. *Cancer Imaging*. 2010;10(SPEC. ISS. A):163-171.

4. Le Bihan D, Breton E, Lallemand D, Grenier P, Cabanis E, Laval-Jeantet M. MR imaging of intravoxel incoherent motions: Application to diffusion and perfusion in neurologic disorders. *Radiology*. 1986;161(2).

5. Merboldt KD, Hanicke W, Frahm J. Self-diffusion NMR imaging using stimulated echoes. *Journal of Magnetic Resonance (1969)*. 1985;64(3).

6. Taylor DG, Bushell MC. The spatial mapping of translational diffusion coefficients by the NMR imaging technique. *Phys Med Biol*. 1985;30(4).

7. Le Bihan D, Mangin JF, Poupon C, et al. Diffusion tensor imaging: Concepts and applications. *Journal of Magnetic Resonance Imaging*. 2001;13(4):534-546.

8. Dietrich O, Biffar A, Baur-Melnyk A, Reiser MF. Technical aspects of MR diffusion imaging of the body. *Eur J Radiol*. 2010;76:314-322.

9. Maurer MH, Heverhagen JT. Diffusion weighted imaging of the prostate-principles, application, and advances. *Transl Androl Urol*. 2017;6(3):490-498.

10. Bourne RM, Bongers A, Chatterjee A, Sved P, Watson G. Diffusion anisotropy in fresh and fixed prostate tissue ex vivo. *Magn Reson Med*. 2016;76(2).

11. Medved M, Soylu-Boy FN, Karademir I, et al. High-resolution diffusion-weighted imaging of the prostate. *American Journal of Roentgenology*. 2014;203(1):85-90.

12. Bihan D Le. Molecular diffusion, tissue microdynamics and microstructure. *NMR Biomed*. 1995;8(7).

13. Boucher S, Arribarat G, Cartiaux B, et al. Diffusion Tensor Imaging Tractography of White Matter Tracts in the Equine Brain. *Front Vet Sci*. 2020;7.

14. Burakiewicz J, Hooijmans MT, Webb AG, Verschuuren JJGM, Niks EH, Kan HE. Improved olefinic fat suppression in skeletal muscle DTI using a magnitude-based dixon method. *Magn Reson Med*. 2018;79(1):152-159.

15. Khalique Z, Ferreira PF, Scott AD, Nielles-Vallespin S, Firmin DN, Pennell DJ. Diffusion Tensor Cardiovascular Magnetic Resonance Imaging: A Clinical Perspective. *JACC Cardiovasc Imaging*. 2020;13(5).

16. Basser PJ, Mattiello J, LeBihan D. MR diffusion tensor spectroscopy and imaging. *Biophys J*. 1994;66(1):259-267.

17. van Gelderen P, de Vleeschouwer MHM, DesPres D, Pekar J, van Zijl PCM, Moonen CTW. Water diffusion and acute stroke. *Magn Reson Med*. 1994;31(2).

18. Van Rijswijk CSP, Kunz P, Hogendoorn PCW, Taminiau AHM, Doornbos J, Bloem JL. Diffusion-weighted MRI in the characterization of soft-tissue tumors. *Journal of Magnetic Resonance Imaging*. 2002;15(3).

19. Andica C, Kamagata K, Hatano T, et al. MR Biomarkers of Degenerative Brain Disorders Derived From Diffusion Imaging. *Journal of Magnetic Resonance Imaging*. 2020;52(6).

20. Connolly M, Srinivasan A. Diffusion-Weighted Imaging in Head and Neck Cancer: Technique, Limitations, and Applications. *Magn Reson Imaging Clin N Am*. 2018;26(1):121-133.

21. Steiger P, Thoeny HC. Prostate MRI based on PI-RADS version 2: How we review and report. *Cancer Imaging*. 2016;16(1).

22. Bharwani N, Koh DM. Diffusion-weighted imaging of the liver: An update. *Cancer Imaging*. 2013;13(2).

23. Stejskal EO, Tanner JE. Spin diffusion measurements: Spin echoes in the presence of a time-dependent field gradient. *J Chem Phys*. 1965;42(1).

24. Godi C, De Vita E, Tombetti E, Davagnanam I, Haddow L, Jäger HR. High b-value diffusion-weighted imaging in progressive multifocal leukoencephalopathy in HIV patients. *Eur Radiol*. 2017;27(9).

25. Jahng GH, Li KL, Ostergaard L, Calamante F. Perfusion magnetic resonance imaging: A comprehensive update on principles and techniques. *Korean J Radiol*. 2014;15(5).

26. Rzedzian R, Mansfield P, Doyle M, et al. REAL-TIME NUCLEAR MAGNETIC RESONANCE CLINICAL IMAGING IN PAEDIATRICS. *The Lancet*. 1983;322(8362).

27. Ordidge R. The development of echo-planar imaging (EPI): 1977–1982. *Magma: Magnetic Resonance Materials in Physics, Biology, and Medicine*. 1999;9(3).

28. Clare S, Jezzard P. Rapid T1 mapping using multislice echo planar imaging. *Magn Reson Med*. 2001;45(4).

29. Schmidt CF, Degonda N, Luechinger R, Henke K, Boesiger P. Sensitivity-encoded (SENSE) echo planar fMRI at 3T in the medial temporal lobe. *Neuroimage*. 2005;25(2).

30. Pruessmann KP, Weiger M, Scheidegger MB, Boesiger P. SENSE: Sensitivity encoding for fast MRI. *Magn Reson Med*. 1999;42(5):952-962.

31. Griswold MA, Jakob PM, Heidemann RM, et al. Generalized Autocalibrating Partially Parallel Acquisitions (GRAPPA). *Magn Reson Med*. 2002;47(6).

32. Wu W, Miller KL. Image formation in diffusion MRI: A review of recent technical developments. *Journal of Magnetic Resonance Imaging*. 2017;46(3):646-662.

33. Buonocore MH, Gao L. Ghost artifact reduction for echo planar imaging using image phase correction. *Magn Reson Med*. 1997;38(1).

34. Buonocore MH, Zhu DC. Image-based ghost correction for interleaved EPI. *Magn Reson Med*. 2001;45(1):96-108.

35. Butts K, Riederer SJ, Ehman RL, Thompson RM, Jack CR. Interleaved Echo Planar Imaging on a Standard MRI System. Published online 1994:67-72.

36. McKinnon GC. Ultrafast interleaved gradient-echo-planar imaging on a standard scanner. *Magn Reson Med*. 1993;30(5):609-616.

37. Andersson JLR, Skare S, Ashburner J. How to correct susceptibility distortions in spin-echo echo-planar images: Application to diffusion tensor imaging. *Neuroimage*. 2003;20(2):870-888.

38. Mugler JP, Brookeman JR. Off-resonance image artifacts in interleaved-EPI and GRASE pulse sequences. *Magn Reson Med*. 1996;36(2):306-313.

39. Jeong HK, Gore JC, Anderson AW. High-resolution human diffusion tensor imaging using 2-D navigated multishot SENSE EPI at 7 T. *MRM*. 2013;69(3):793-802.

40. Porter DA, Heidemann RM. High resolution diffusion-weighted imaging using readout-segmented echo-planar imaging, parallel imaging and a two-dimensional navigator-based reacquisition. *Magn Reson Med*. 2009;62(2).

41. Dong Y, Koolstra K, Riedel M, van Osch MJP, Börnert P. Regularized joint water–fat separation with B0 map estimation in image space for 2D-navigated interleaved EPI based diffusion MRI. *Magn Reson Med*. 2021;86(6):3034-3051.

42. Krinsky G, Rofsky NM, Weinreb JC. Nonspecificity of short inversion time inversion recovery (STIR) as a technique of fat suppression: Pitfalls in image interpretation. *American Journal of Roentgenology*. 1996;166(3).

43. Zee CS, Segall HD, Terk MR, et al. SPIR MRI in spinal diseases. *J Comput Assist Tomogr*. 1992;16(3):356-360.

44. Kaldoudi E, Williams SCR, Barker GJ, Tofts PS. A chemical shift selective inversion recovery sequence for fat-suppressed MRI: Theory and experimental validation. *Magn Reson Imaging*. 1993;11(3).

45. Steinhoff M, Nehrke K, Mertins A, Börnert P. Segmented diffusion imaging with iterative motion-corrected reconstruction (SEDIMENT) for brain echo-planar imaging. *NMR Biomed*. 2020;33(12):e4185.

46. Guhaniyogi S, Chu ML, Chang HC, Song AW, Chen NK. Motion immune diffusion imaging using augmented MUSE for high-resolution multi-shot EPI. *Magn Reson Med*. 2016;75(2):639-652.

47. Guo H, Ma X, Zhang Z, Zhang B, Yuan C, Huang F. POCS-enhanced inherent correction of motion-induced phase errors (POCS-ICE) for high-resolution multishot diffusion MRI. *Magn Reson Med*. 2016;75(1):169-180.

48. Chen N kuei, Guidon A, Chang HC, Song AW. A robust multi-shot scan strategy for high-resolution diffusion weighted MRI enabled by multiplexed sensitivity-encoding (MUSE). *Neuroimage*. 2013;72:41-47.

49. Hu Y, Wang X, Tian Q, et al. Multi-shot diffusion-weighted MRI reconstruction with magnitude-based spatial-angular locally low-rank regularization (SPA-LLR). *Magn Reson Med*. 2020;83(5):1596-1607.

50. Hu Y, Levine EG, Tian Q, et al. Motion-robust reconstruction of multishot diffusion-weighted images without phase estimation through locally low-rank regularization. *Magn Reson Med*. 2019;81(2):1181-1190.

51. Mani M, Jacob M, Kelley D, Magnotta V. Multi-shot sensitivity-encoded diffusion data recovery using structured low-rank matrix completion (MUSSELS). *Magn Reson Med*. 2017;78(2):494-507.

52. Mani M, Aggarwal HK, Magnotta V, Jacob M. Improved MUSSELS reconstruction for high-resolution multi-shot diffusion weighted imaging. *Magn Reson Med*. 2020;83(6):2253-2263.

53. Ren J, Dimitrov I, Sherry AD, Malloy CR. Composition of adipose tissue and marrow fat in humans by 1H NMR at 7 Tesla. *J Lipid Res*. 2008;49(9):2055-2062.

54. Hamilton G, Yokoo T, Bydder M, et al. In vivo characterization of the liver fat 1H MR spectrum. *NMR Biomed*. 2011;24(7):784-790.

55. Frahm J, Merboldt KD, Hänicke W. Localized proton spectroscopy using stimulated echoes. *Journal of Magnetic Resonance (1969)*. 1987;72(3):502-508.

56. Ma J. Dixon techniques for water and fat imaging. *Journal of Magnetic Resonance Imaging*. 2008;28(3):543-558.

57. Yu H, Reeder SB, Shimakawa A, Brittain JH, Pelc NJ. Field map estimation with a region growing scheme for iterative 3-point water-fat decomposition. *Magn Reson Med*. 2005;54(4):1032-1039.

58. Hu HH, Börnert P, Hernando D, et al. ISMRM workshop on fat-water separation: Insights, applications and progress in MRI. *Magn Reson Med*. 2012;68(2):378-388.

59. Reeder SB, Pineda AR, Wen Z, et al. Iterative decomposition of water and fat with echo asymmetry and least-squares estimation (IDEAL): Application with fast spin-echo imaging. *Magn Reson Med*. 2005;54(3):636-644.

60. Uecker M. Making SENSE of Chemical Shift: Separating Species in Single-Shot EPI using Multiple Coils. *ISMRM*. 2012;20:2490.